Journal of Alloys and Compounds 863 (2021) 158320

Contents lists available at ScienceDirect

Journal of Alloys and Compounds

journal homepage: www.elsevier.com/locate/jalcom

Influence of reducing heat treatment on the structural and magnetic properties of MnO:ZnO ceramics

V.M. Almeida Lage[a], R.T. da Silva[a], A. Mesquita[b], M.P.F. de Godoy[c], X. Gratens[d], V.A. Chitta[d], H.B. de Carvalho[e,*]

[a] Universidade Federal de Ouro Preto – UFOP, 35400-000 Ouro Preto, MG, Brazil
[b] Departamento de Física, Instituto de Geociências e Ciências Exatas, Universidade Estadual Paulista – UNESP, 13500-900 Rio Claro, Brazil
[c] Departamento de Física, Universidade Federal de São Carlos – UFSCar, 13565-905 São Carlos, Brazil
[d] Instituto de Física, Universidade de São Paulo – USP, 05508-090 São Paulo, Brazil
[e] Universidade Federal de Alfenas – UNIFAL, 37130-000 Alfenas, Brazil

ARTICLE INFO

Article history:
Received 1 October 2020
Received in revised form 5 December 2020
Accepted 11 December 2020
Available online 10 January 2021

Keywords:
Multifunctionality
Spintronics
Zinc oxide
Defect engineering

ABSTRACT

Polycrystalline MnO:ZnO bulk ceramics with a Mn proportion of 6, 11, 17 and 22 at% are prepared through a solid-state reaction and subjected to a heat treatment in a reducing atmosphere (Ar (95%) and H_2 (5%)). The samples are studied with particular emphasis on their composition and structural and magnetic properties. A detailed microstructural and chemical analysis confirms the Mn doping of the wurtzite ZnO structure mainly at the surface of the ZnO grains. For the samples with higher Mn proportions, the secondary phases $ZnMn_2O_4$ and $Mn_{1-x}Zn_xO$ (Zn-doped MnO) are detected for the as-prepared and heat-treated samples, respectively. The structural change of the secondary phases under heat treatment, from $ZnMn_2O_4$ to $Mn_{1-x}Zn_xO$, confirms the effectiveness of the heat treatment in reducing the valence of the Mn ions and in the formation of oxygen vacancies into the system. In spite of the induced defects, the magnetic analysis presents only a paramagnetic behavior with an antiferromagnetic coupling between the Mn ions. In the context of the bound magnetic polaron theory, it is concluded that oxygen vacancies are not the necessary defect to promote the desired ferromagnetic order at room temperature.

1. Introduction

ZnO is a truly multifunctional material [1,2] and, as a nontoxic abundant resource with excellent environmental affinity, has received significant attention in recent decades. With a wide bandgap (3.4 eV) and a strong exciton binding energy (60 meV) at room temperature [3], ZnO has been explored in different applications and technologies, including photocatalysis [4], energy harvesting devices [5], gas sensing systems [6,7] and photovoltaic elements [8]. The functionalization of ZnO is mainly achieved via defect engineering, by doping or even by the introduction of defects into the structural lattice in a well-controlled manner [9].

The magnetic properties of ZnO are also of remarkable interest. ZnO is a diamagnetic material and its magnetic functionalization takes place via doping with magnetic elements or by associating it to magnetic materials in the form of a core-shell system [10]. Magnetic ZnO at the nanoscale has been explored in biomedicine as a bioimaging and drug delivery agent [10], as well as in antibacterial complexes [11]. In addition, magnetic ZnO is also a promising dilute magnetic semiconductor (DMS) that can be used as a spin injection layer in spintronic devices [12]. Research on transitional metal (TM)-doped ZnO for spintronic purposes was inspired after the theoretical study of Dietl et al. [13]. According to these authors, wide band gap semiconductors, such as Mn-doped ZnO and GaN, show Curie temperatures (T_C) above room temperature and therefore present room temperature ferromagnetism (RTFM). However, in spite of experimental and theoretical efforts in recent decades, our knowledge regarding the magnetic properties of such materials, especially concerning TM-doped oxides, is still debated and inconclusive. Currently, there is a consensus that TM doping of oxide structures is not sufficient and structural defects also play an important role in tuning the functional properties of the oxides, particularly their magnetic properties [14–18].

Considering the case of TM-doped ZnO, there are several literature reports that connect an observed RTFM to different structural point defects, such as zinc vacancies (V_{Zn}) [19,20], zinc interstitials

* Corresponding author.
E-mail address: hugo.carvalho@unifal-mg.edu.br (H.B. de Carvalho).

https://doi.org/10.1016/j.jallcom.2020.158320
0925-8388/

(Zn_i) [17,21] and oxygen vacancies (V_O) [22,23]. Among these defects, V_O are widely believed to have a major role in promoting the desired RTFM [23–27]. A common technique to promote the formation of V_O in the wurtzite ZnO (*w*-ZnO) structure is heat treatment in a low-oxygen [28,29], inert [30,31] or reducing atmosphere [31–37]. Eq. (1) illustrates the formal reaction [38–41] in the case of heat treatment with hydrogen (H_2). Nevertheless, under heating, the vaporization of ZnO takes place predominantly via dissociation into gaseous Zn and O_2 [41] and therefore the heat treatment also promotes defects at Zn sites, in addition to V_O. For instance, Meng et al. [42] showed that Al and Mg co-doped *w*-ZnO under heat treatment in forming gas (97% N_2 and 3% H_2) at 650 °C for 1 h can completely remove Zn from the samples and leaving a dominant Mg oxide phase remaining.

$$ZnO\ (s) + H_2 \rightarrow Zn_{Zn} + V_O^{\bullet\bullet} + 2e' + H_2O\ (g) \quad (1)$$

From a theoretical point of view, different models have been proposed to explain the typically observed RTFM in DMSs. The main accepted model for insulating systems is the bound magnetic polaron (BMP) theory proposed by Coey et al. [43], who argued that the ferromagnetic exchange coupling among TM dopants is mediated by shallow donor electrons. These defects form bound magnetic polarons that overlap to create a spin-split impurity band. Since V_O are theoretically predicted to be deep donor defects in *w*-ZnO [44], they can be associated to the observed RTFM under the scope of the BMP model. In spite of this, highly stable polarons can also be formed by holes bound to acceptor defects in oxides [45,46], meaning that magnetic polarons can therefore also be formed in insulating doped DMSs [47], including TM-doped *w*-ZnO [48]. Therefore, V_{Zn}, as shallow acceptor defects [44], also have to be considered as a necessary defect for the promotion of RTFM in the context of the BMP model.

In this scenario, one can address the controversy regarding the magnetic properties of these systems to the lack of knowledge in the nature and control of the densities of defects in the studied materials. The aim of the present study is to further contribute to the understanding of Mn incorporation into the *w*-ZnO structure and provide insight into the nature of the necessary defects to promote and stabilize the desired RTFM in ZnO-based DMSs. Mn, as a TM element with an electron configuration of [Ar] $4s^2\ 3d^5$ (high spin), can add the necessary spins to confer the desired ferromagnetic order (RTFM) to the system. However, as discussed, to achieve this objective, we must ensure a ferromagnetic coupling among the Mn spins, which can be accomplished adding by the appropriate point defects to the *w*-ZnO structure based on the BMP model. Mn can assume a 2+ oxidation state and can easily replace the Zn^{2+} ion in the *w*-ZnO lattice via substitutional doping. Under this condition, the Mn^{2+} ions at the Zn^{2+} tetrahedral sites of the wurtzite structure have an ionic radius of 0.66 Å [49], which is slightly larger than the ionic radius of 0.60 Å for Zn^{2+} [49]. Therefore, the incorporation of Mn^{2+} ions into the *w*-ZnO structure inevitably introduces structural distortions (with an increase in the cell parameters), as reported by Kolesnik et al. [50]. This leads to a relatively lower Mn^{2+} solubility limit in *w*-ZnO (< 0.05) for the standard sintering process in air [51].

In this study, we conduct a detailed analysis of the microstructural and magnetic properties of MnO:ZnO bulk samples prepared by a standard solid-state reaction method. The samples are sintered under an oxygen atmosphere, fractions of the samples are then subjected to a heat treatment in a reducing atmosphere of Ar (95%) and H_2 (5%) in order to introduce defects through a controlled approach. We find that, in spite of having induced V_O in the *w*-ZnO structure via the reducing heat treatment, the samples only present paramagnetic behavior with an antiferromagnetic interaction among the Mn ions.

2. Experimental

Polycrystalline MnO:ZnO bulk ceramic samples were prepared via a standard solid-state reaction method considering the atomic ratio (*x*) between the number of Mn (N_{Mn}) atoms and the total number of cations in the samples ($N_{Mn} + N_{Zn}$), $x = N_{Mn}/(N_{Mn} + N_{Zn})$. Appropriate amounts of ZnO (Alfa Aesar 99.999% purity) and MnO (Alfa Aesar 99.99% purity) powders were mixed with $x = 0.06$ (labeled as MnZn06), 0.11 (MnZn11), 0.17 (MnZn17) and 0.22 (MnZn22). The powders were ball milled for 5 h using Zn spheres and the resulting mixtures were cold compacted at 600 MPa in the form of pellets (green pellets). The green pellets were finally sintered in a tubular oven at 1400 °C for 4 h in a dynamic atmosphere of oxygen with a flow rate of 2 L/min. These samples were labeled as as-prepared (*AP*). Fractions of these samples were then heat-treated in a dynamic reducing atmosphere of Ar (95%) and H_2 (5%) (Ar + H_2) at 600 °C for 3 h with a gas flow rate of 1.5 L/min. These samples were labeled as heat-treated (*HT*). The sintering and heat treatment processes were performed at a heating and cooling rates of 10 °C/min. Three pellets of each proportion *x* were prepared and measured in order to test the reproducibility of the experimental results. Fig. 1 presents a flowchart of the procedure employed in the preparation and characterization of the samples.

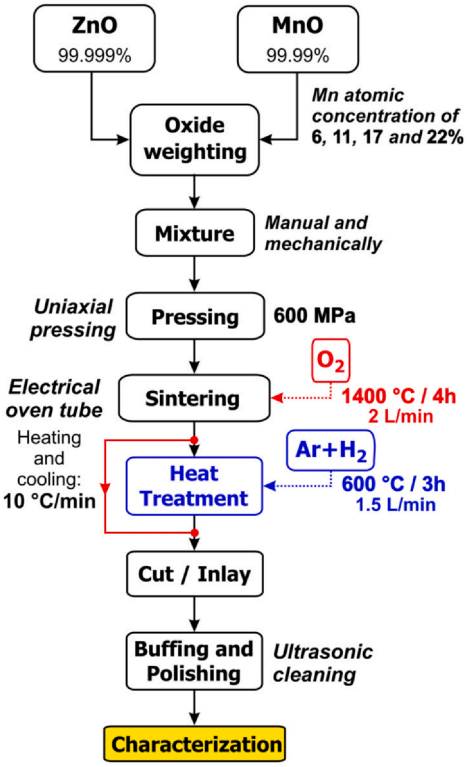

Fig. 1. Flowchart of the preparation of the polycrystalline MnO:ZnO bulk samples.

The structural characterization of the MnO:ZnO samples was performed via powder X-ray diffraction (XRD) using a Rigaku Ultima IV diffractometer, employing Cu-Kα radiation (30 kV, 40 mA, λ = 1.5418 Å) and recorded in the range of 2θ = 15–120° with steps of 0.02° at 7 s/step. The determination of the lattice parameters and the occupation factor over the structure were evaluated using the Rietveld method implemented via the General Structure Analysis System with the graphical user interface EXPGUI [52,53]. The microstructure was determined using scanning electron microscopy (SEM) with a LV JEOL JSM 6510 and a resolution of 3 nm at 30 kV. The effective Mn concentration (x_E) incorporated into the *w*-ZnO structure was estimated by energy-dispersive X-ray spectroscopy (EDS) using an Oxford XMAX 50 detector. Raman scattering spectroscopy was employed to study the incorporation of Mn and the resulting lattice disorder in the *w*-ZnO host structure, as well as to analyze the formation of segregated secondary phases. Raman measurements were acquired using an IHR-550 Horiba Jobin Yvon spectrometer equipped with a Synapse charge coupled device detector and an

Olympus BX41 microscope, and by using 10× and 100× objective lenses in the backscattering configuration. The spectra were collected at several different points for each sample in order to enhance the statistical analysis. The excitation was performed with a 532 nm wavelength laser and a laser power of 1 mW over the sample. X-ray absorption spectroscopic analysis was employed to determine the oxidation state (X-ray near-edge spectroscopy (XANES)) and to assess the environment (extended X-ray absorption fine structure (EXAFS)) of the Mn atoms in the MnO:ZnO samples. These measurements were performed at the Mn and Zn *K*-edge in transmission mode using a Si (111) channel-cut monochromator at the XAFS2 beamline of the Brazilian Synchrotron Light Laboratory (LNLS). Finally, temperature-dependent (3–300 K) magnetic measurements were performed using a Cryogenics superconducting quantum interference device (SQUID) magnetometer in DC mode in magnetic fields up to 6 T.

3. Results and discussion

3.1. X-ray diffraction

Fig. 2 shows the XRD results for the MnO:ZnO samples. The main observed peaks correspond to those expected for polycrystalline hexagonal *w*-ZnO (space group $P6_3mc$, PDF 01-072-8025) [54]. The relatively narrow line widths revealed a high crystalline quality for all samples. For the samples MnZn06, *AP* and *HT*, no additional phases were observed within the detection limit of the measurements. However, for the other samples ($x > 0.06$), we observe the presence of secondary phases: zinc (II) dimanganate ($ZnMn_2O_4$) for the *AP* samples and manganese (II) oxide (MnO) for the *HT* samples (symbols in Fig. 2). The $ZnMn_2O_4$ phase has a tetragonal spinel structure (AB_2O_4) in which the Zn^{2+} occupies the AO_4 tetrahedral sites (T_d) and the Mn^{3+} occupies the BO_6 octahedral sites (O_h). The crystal structure of $ZnMn_2O_4$ spinel belongs to the $I4_1/adm$ space group. In addition, MnO has a cubic rock-salt structure with Mn^{2+} ions at octahedral sites (space group $Fm\bar{3}m$). This result indicates, as expected, a reduction in the oxidation state of Mn^{3+} to Mn^{2+} with the heat treatment in the Ar + H_2 atmosphere. Sharma et al. report the presence of $ZnMn_2O_4$ for MnO_2:ZnO samples sintered in air at 800 °C and the MnO phase after heat treatment in Ar (90%) and H_2 (10%) at 800 °C [34]. Kolesnik et al. also observed the same secondary phase of $ZnMn_2O_4$ for MnO_2:ZnO samples sintered in air at 1350 °C [55].

The obtained Rietveld structural parameters are presented in the supplementary information (Figs. S1 and S2 and Tables S1 and S2). The main results concern the calculation of the fraction of the phases (*w*-ZnO, $ZnMn_2O_4$ and MnO) and the site occupation factors for each element in each phase. As *x* increases, the diffraction peaks corresponding to the secondary phases increase with respect to the peaks of the *w*-ZnO structure. The refined fraction of the phases revealed a linear behavior with *x* (Fig. S3(a)). It is noteworthy that there is a small remaining fraction of $ZnMn_2O_4$ in the *HT* samples (Table S2).

The refined occupation factor for the Mn in the *w*-ZnO matrix, addressed as x_R, is presented in Table 1. First, we observe that x_R is in good agreement with the effective Mn concentration (x_E) measured via EDS (Table 1) and that it increases as *x* increases. The incorporation of Mn ions into the *w*-ZnO lattice is corroborated by the linear increase of the refined volume of the *w*-ZnO unit cell of the $Zn_{1-x}Mn_xO$ phase as a function of x_R, as expected under Vegard's law (Fig. S3(b)), and by the trend of the increasing of the calculated strain (ε) (Table S3). For the *HT* samples, the strain is somewhat smaller than that for the *AP* samples, revealing that the heat treatment also induces strain relief in the structure of the samples, as in an annealing process. The increase of the incorporated Mn concentration (x_R) into *w*-ZnO can be further interpreted as a function of the changes in the grain growth conditions in the presence of successively higher amounts of the MnO precursor in each sample.

3.2. Electron microscopy and elemental analyses

Fig. 3(a) and (b) show representative SEM images acquired over the polished surface of the MnO:ZnO samples. The images were obtained using a backscattered electron detector in order to highlight the secondary phases of $ZnMn_2O_4$ (*AP*) and MnO (*HT*). An increase in the number and size of the secondary phases (dark gray grains in Fig. 3(a) and (b)) is observed at the microscale as *x* increases, in accordance with the XRD and Rietveld results. A series of full scans over large areas of the MnZn06 *AP* and *HT* samples also reveals the presence of a very small amount of secondary phases not detected using XRD (red arrows in Fig. 3). This finding can explain, in part, the slightly lower values obtained for x_R and x_E as compared to *x* (Table 1). This observation also highlights the limitation of XRD in detecting secondary phases even at the microscale. For instance, in the context of developing true DMSs, it is hard important to exclude the presence of any magnetic secondary phases that could lead to misinterpretations regarding the magnetic behavior. Therefore, for this purpose, it is necessary always to conjugate different experimental techniques and use highly sensitive tools at the nanoscale.

Elemental analyses were performed via EDS measurements at multiple points and also over large surface areas of the samples. Representative EDS maps and point spectra measured at Zn- and Mn-rich grains (open and full cross in panel MnZn22 in Fig. 3,

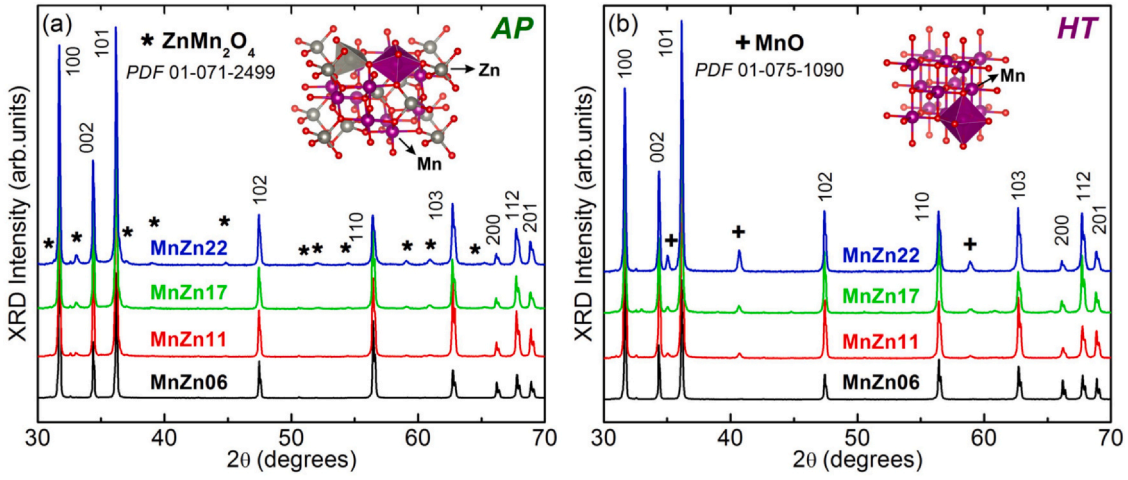

Fig. 2. XRD patterns of the polycrystalline MnO:ZnO bulk samples prepared with different Mn concentrations for the (a) *AP* and (b) *HT* samples. Stars show the peak positions of the secondary $ZnMn_2O_4$ phase in (a) and crosses show the peak positions of the MnO secondary phase in (b).

Table 1
Mn effective concentration (x_E) measured by EDS and obtained via Rietveld refinement (x_R). The presented error for the x_E data corresponds to the standard error of the mean. For the $ZnMn_2O_4$ phase in the *AP* samples and for the MnO phase in the *HT* samples, we also present the Zn concentration (x_{Zn}) for comparison.

Sample	AP				HT			
	$Zn_{1-x}Mn_xO$		$ZnMn_2O_4$		$Zn_{1-x}Mn_xO$		$Mn_{1-x}Zn_xO$	
	x_R	x_E	Zn	Mn	x_{Zn}	x_R	x_E	x_{Zn}
MnZn06	0.041(3)	0.054(9)	0.16(1)	0.27(1)	0.37(1)	0.044(1)	0.053(6)	0.38(2)
MnZn11	0.071(1)	0.069(6)	0.16(2)	0.27(2)	0.37(1)	0.062(2)	0.07(1)	0.42(4)
MnZn17	0.079(2)	0.080(5)	0.16(2)	0.27(2)	0.37(1)	0.076(2)	0.077(6)	0.34(4)
MnZn22	0.094(1)	0.088(5)	0.15(2)	0.28(2)	0.39(2)	0.079(3)	0.084(5)	0.42(4)

respectively) are also presented in Figs. S4 and S5. The obtained average elemental percentages (x_E) are listed in Table 1. We could confirm Mn doping of the *w*-ZnO lattice for all samples, leading us to nominate this phase as $Zn_{1-x}Mn_xO$ in Table 1. We observe that x_E increases as x increases and, as discussed previously, x_E is in good agreement with the x_R factor obtained from the Rietveld analyses. It is stated that x_R and x_E correspond to the Mn limit of solubility in the *w*-ZnO lattice under the preparation conditions used in this study.

We also call attention to the Zn that is present in the MnO phase (Fig. S5(f)), since the structure of this phase corresponds to that of MnO, meaning that the Zn atoms are incorporated into the MnO lattice, i.e., a Zn-doped MnO phase. Therefore, we nominate this secondary phase more properly as $Mn_{1-x}Zn_xO$. As can be seen in Table 1, the Zn fraction in the MnO secondary phase matrix (x_{Zn}) is almost the same as the Zn fraction in the $ZnMn_2O_4$ secondary phase in the *AP* samples (also labeled as x_{Zn} in Table 1). This finding leads us to conclude that the performed heat treatment in the reducing atmosphere (Ar + H_2) is effective in removing oxygen atoms from the samples. The $ZnMn_2O_4$ phase is, therefore, induced to a structural change to $Mn_{1-x}Zn_xO$ due to the high amount of oxygen vacancies (V_O) promoted under the heat treatment.

On the same basis, but to a lesser extent, we can infer that with the heat treatment, V_O were also promoted in the Mn-doped *w*-ZnO ($Zn_{1-x}Mn_xO$) main fraction of the samples. Singhal et al. showed, via X-ray photoelectron spectroscopy, the induction of V_O after heat treatment in hydrogen at 500 °C for 6 h for MnO_2:ZnO samples previously sintered in two steps in air at 600 °C (first step) and 500 °C (second step) [56].

Table 2 presents the parameters obtained after a statistical analysis for the grain diameter distribution. The histogram for each sample is presented in Figs. S6 and S7. We observe that as x increases, the main diameter (d) of the grains decreases. It is well known that secondary phase particles can inhibit grain growth by pinning/dragging the migration of grain boundaries, which is often known as the Zener effect [57]. Since a growing amount of secondary phases ($ZnMn_2O_4$) is observed in the *AP* samples with increasing MnO, we can state that the formed $ZnMn_2O_4$ grains act as pinning/dragging centers that inhibit the *w*-ZnO grain growth, leading to a decrease in d as a function of x. With this result, we can return to the observed increasing of the Mn content (x_R and x_E) into the *w*-ZnO matrix as a function of x. We can infer here that the incorporation of the Mn ions into the *w*-ZnO takes place mainly at the grain surfaces. Increasing the MnO precursor proportion in the preparation of the MnO:ZnO ceramics (increasing x), the proportion of the $ZnMn_2O_4$ in the *AP* samples also increases, leading to a decrease of the *w*-ZnO mean grain diameter (d), which, in turn, leads to an increase in the effective total surface area in the samples, therefore allowing for higher Mn incorporation. It is import to stress here that similar results were also reported for Mn-doped nanograined *w*-ZnO samples [58].

Table 2
Particle size distribution analyses, where d is the mean value of the particle diameter, σ_g is the geometric standard deviation obtained by the log-normal fit of particle size distribution histograms for each sample and N is the total number of counted particles.

Sample	*AP*			*HT*		
	d (μm)	σ_g	N	d (μm)	σ_g	N
MnZn06	40.0(6)	1.49(1)	221	38.7(8)	1.49(2)	261
MnZn11	24.7(2)	1.37(1)	278	26.6(2)	1.37(1)	287
MnZn17	20.0(2)	1.38(1)	358	20.9(4)	1.52(2)	390
MnZn22	17.0(2)	1.43(1)	254	18.8(2)	1.49(1)	337

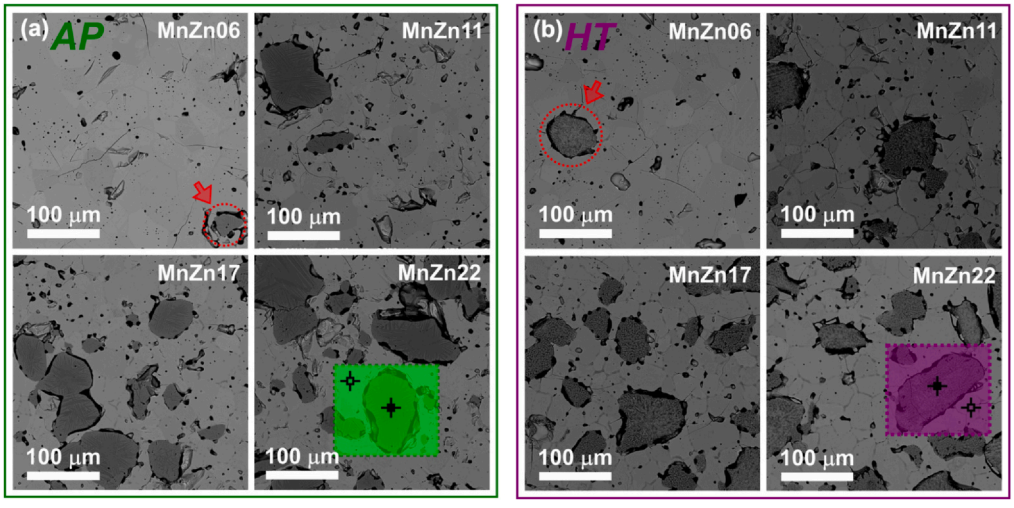

Fig. 3. Representative SEM images obtained from the backscattered configuration of the polycrystalline bulk (a) *AP* and (b) *HT* samples MnZn06 (x = 0.06), MnZn11 (0.11), MnZn17 (0.17) and MnZn22 (0.22). The secondary phase is well observed in the panels as dark gray grains. Highlighted areas in the panels for MnZn22 correspond to the area where the EDS mapping was conducted (Figs. S4 and S5). (For interpretation of the references to color in this figure legend, the reader is referred to the web version of this article.)

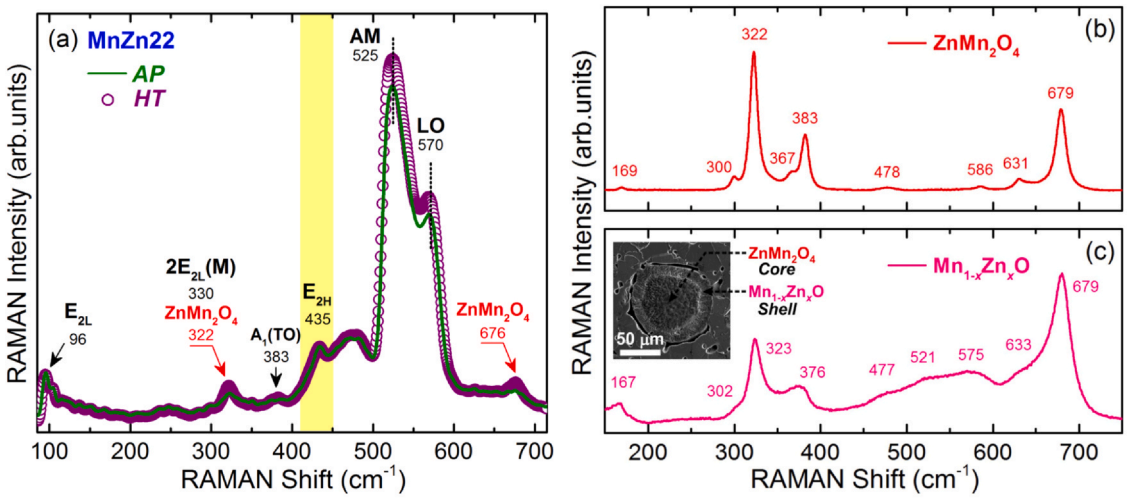

Fig. 4. (a) Raman scattering spectra of MnZn22 ($x = 0.22$) *AP* and *HT* samples. The spectra were acquired at room temperature and are normalized by the main vibrational mode E_{2H}. The spectrum for the *AP* sample is shown in solid lines and the symbols correspond to the spectrum for the *HT* sample. Raman scattering spectrum acquired (b) for $ZnMn_2O_4$ (*AP*) and (c) $Mn_{1-x}Zn_xO$ (*HT*). The inset in (c) shows a representative SEM image of a relatively large core-shell grain formed by a $ZnMn_2O_4$ core and a $Mn_{1-x}Zn_xO$ shell. The phase identification was performed via EDS.

3.3. Raman scattering spectroscopy

Raman scattering measurements were performed in order to achieve a detailed structural analysis and evaluate the chemical composition of the samples. Fig. 4(a) shows a representative spectrum for the MnZn22 *AP* and *HT* samples. The spectra for the other samples are quite similar to those shown in Fig. 4(a). The Raman spectrum were measured here using an objective of 10×, which leads to a relatively high analyzed average area. The presented spectrum corresponds also to an average of spectra acquired at several different points over the polished surface of the samples. The series of narrow modes centered at 97, 383 and 435 cm^{-1} are assigned to the E_{2L}, A_1(TO) and E_{2H} modes of the *w*-ZnO lattice, respectively [59]. In Fig. 4(a) the spectra are normalized by the integrated intensity of the main mode E_{2H}. We also observe an extrinsic broad band between 500 and 600 cm^{-1}, which seems to be formed by the overlapping of several vibrational modes, with the most intense ones centered at 525 and 570 cm^{-1}. The mode at 570 cm^{-1} can be attributed to the overlap of the A_1(LO) and E_1(LO) modes of the *w*-ZnO lattice [60]. These modes usually present low intensities in undoped *w*-ZnO systems due to the destructive interference between the deformation and the Frölich potentials [61]. In contrast, the vibrational mode at 525 cm^{-1} cannot be attributed to the *w*-ZnO structure.

The emergence of this broad band is well reported in the literature for undoped [62,63] and doped *w*-ZnO with different elements [64–69], including Mn [18,70]. This band is clearly caused by the structural disorder induced by the incorporation of dopants and defects into the *w*-ZnO lattice. Therefore, the observation of this extrinsic broad band for our samples is an indication that at least a fraction of the Mn ions of the MnO precursor is incorporated into the *w*-ZnO lattice, thereby corroborating the XRD, Rietveld and EDS analysis. The higher relative intensity of the extrinsic band for *HT*

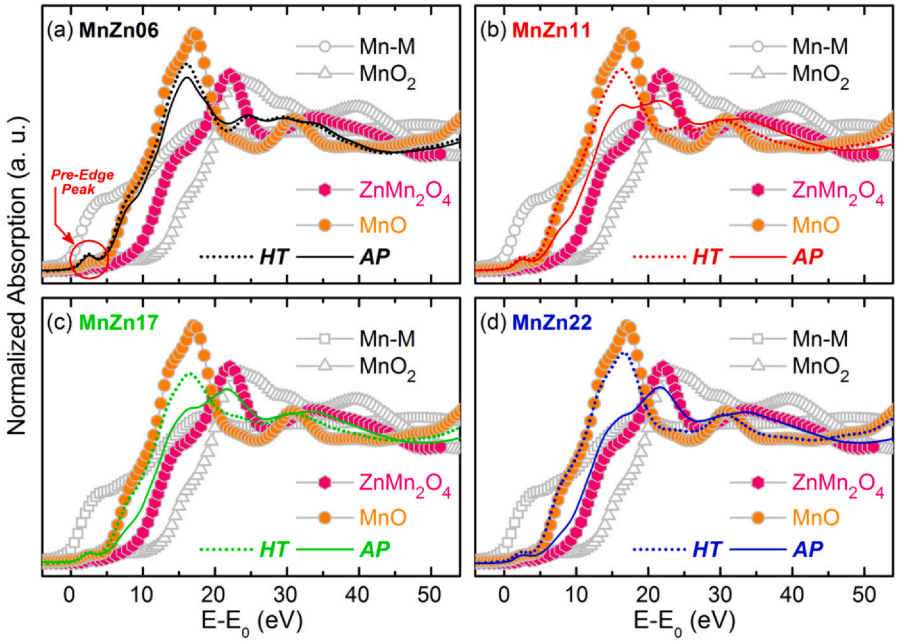

Fig. 5. Mn *K*-edge XANES spectra for the *AP* and *HT* polycrystalline MnO:ZnO bulk samples: (a) MnZn06 ($x = 0.06$), (b) MnZn11 (0.11), (c) MnZn17 (0.17) and (d) MnZn22 (0.22). Spectra of metallic Mn (Mn-M), rocksalt MnO (Mn^{2+}), $ZnMn_2O_4$ (Mn^{3+}) and MnO_2 (Mn^{4+}) are also shown for comparison (E_0 = 6539 eV).

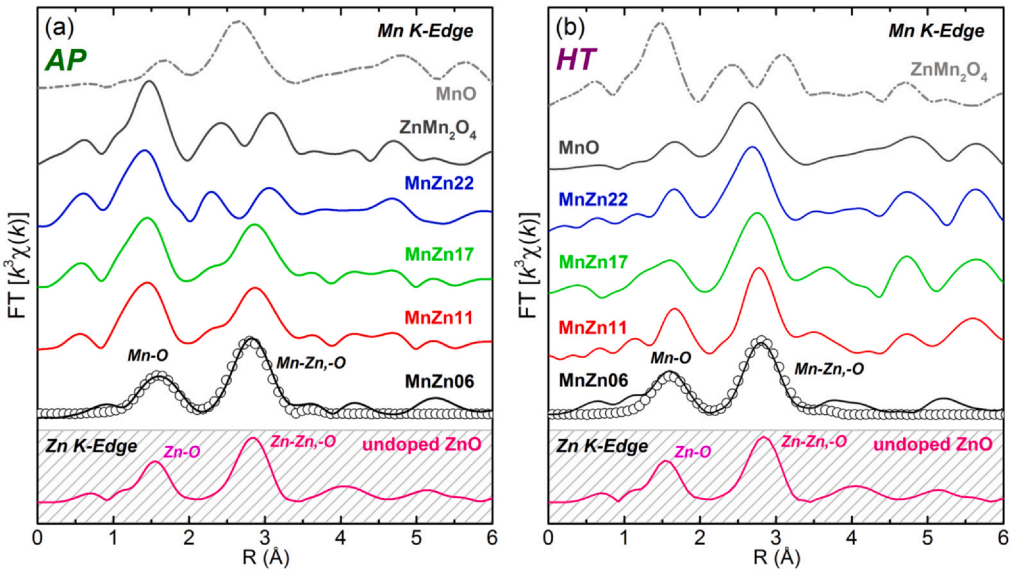

Fig. 6. k^3 weighted Fourier transforms of Mn *K*-edge absorption data for the (a) *AP* and (b) *HT* polycrystalline MnO:ZnO bulk samples and reference powders ($ZnMn_2O_4$ and MnO). The Fourier transforms for the undoped ZnO sample were acquired the Zn *K*-edge. The spectra are offset for clarity. The lines correspond to the experimental data and the symbols correspond to the simulation results.

samples is also noteworthy. Considering that both samples have the same Mn proportions (x_E and x_R in Table 1), we can state that the *HT* samples have a higher density of defects, such as V_O, than the *AP* samples, confirming the previous assumption that the heat treatment in the reducing atmosphere is also effective in introducing these kinds of defects in the Mn-doped *w*-ZnO lattice.

Fig. 4(b) and (c) show representative Raman spectra for the segregated phases $ZnMn_2O_4$ and $Mn_{1-x}Zn_xO$ for the MnZn22 samples, respectively. The spectra were acquired with an objective of 100×, which allows for a high spatial resolution. The obtained spectrum for the $ZnMn_2O_4$ phase of the *AP* samples is in reasonably good agreement with that reported for single phase $ZnMn_2O_4$ samples [71,72]. At the Γ point of the Brillouin zone (*BZ*), group theory predicts ten allowed optical phonons for $ZnMn_2O_4$ represented by $\Gamma = 2A_{1g} + 3B_{1g} + B_{2g} + 4E_g$ [71]. The high-frequency modes (586, 631 and 679 cm^{-1}) are usually associated with the oxygen motion in the tetrahedral AO_4 sites, while the low-frequency modes are associated with the octahedral BO_6 sites [73]. Nevertheless, further studies are necessary in order to corroborate this assumption.

The Raman spectrum for the $Mn_{1-x}Zn_xO$ phase of the *HT* samples (Fig. 4(c)) resembles the spectrum for the $ZnMn_2O_4$ phase (Fig. 4(b)). As presented previously, MnO has a cubic rock-salt structure and it therefore should not exhibit any first-order Raman activity. As a result, we can infer that the structural change of $ZnMn_2O_4$ to $Mn_{1-x}Zn_xO$ under heat treatment is not complete for some $ZnMn_2O_4$ grains. This means that there is some amount of $ZnMn_2O_4$, not detected via XRD in or close to the $Mn_{1-x}Zn_xO$ grains of the *HT* samples. In fact, we could observe an incomplete phase change in some relatively large secondary phase grains in the *HT* samples. The inset of Fig. 4(c) shows a representative SEM image of the secondary phase grains with a core-shell structure formed by a $ZnMn_2O_4$ core and a $Mn_{1-x}Zn_xO$ shell. In addition, the main modes at 322 and 679 cm^{-1} of $ZnMn_2O_4$ are also detected in the spectra presented in Fig. 4(a). It is important to remember that in the region of 330 cm^{-1} for *w*-ZnO, we can find also a relatively lower intensity *w*-ZnO vibrational mode $2E_{2L}$ at the M-point of the *BZ* [74].

3.4. X-ray absorption spectroscopy

Fig. 5 shows the XANES spectra obtained at room temperature for the polycrystalline MnO:ZnO bulk samples at the Mn absorption *K*-edge (6539 eV). It also presents the spectra for different Mn-based reference materials with different Mn oxidation states (metallic Mn and MnO_2) and for the observed secondary phases $ZnMn_2O_3$ and MnO. A XANES spectrum gives information on the coordination symmetry and the valence of ions in a solid. The valence of the dopant ions can be analyzed by comparing their resulting edge structures to those obtained from reference samples.

For the MnZn06 *AP* and *HT* samples (Fig. 5(a)), we observe that the Mn ions mainly assume the +2 oxidation state. The line shape of an absorption spectrum depends on the unfilled local density of states and the coordination symmetry of the absorbing element [16,75]. Here, we observe that the line shape for MnZn06 resembles previously reported spectra for Mn-doped *w*-ZnO [18], indicating that the main fraction of the Mn^{2+} ions occupies the Zn^{2+} sites in the *w*-ZnO lattice (substitutional doping). It is also important to draw attention to the relatively higher white line (maximum after absorption edge) for the *HT* sample. This behavior is directly associated with an increase in the empty states left by open bonds due to vacancies promoted by the heat treatment. This result corroborates the data obtained from Raman spectroscopy concerning the introduction of defects via heat treatment in the Mn-doped *w*-ZnO lattice.

By increasing *x*, it can be observed that the spectra for the *AP* samples approach the spectrum for $ZnMn_2O_4$, not only in the edge, but also in the oscillations above the edge. Similarly, as *x* increases, the spectra for the *HT* samples approach the spectrum for the reference MnO, as expected. Another relevant point concerns the observation of a small pre-edge absorption peak for all the samples (indicated at Fig. 5(a)). This is only possible if Mn^{2+} ions are located in sites without an inversion center of symmetry, like the tetrahedral Zn^{2+} sites in the *w*-ZnO lattice [18,67], instead of the octahedral sites in the $ZnMn_2O_4$ and MnO structures (inserted structures in Fig. 2). This result confirms the previous assumption that a fraction of Mn ions takes the place of Zn^{2+} ions in the *w*-ZnO lattice even for the samples with $x > 0.06$.

Fig. 6 presents the extracted k^3-weighted Fourier transforms of the polycrystalline MnO:ZnO bulk samples, the reference powders of $ZnMn_2O_4$ and MnO, as well as a spectrum obtained at Zn *K*-edge for an undoped ZnO reference sample prepared in the same condition as the *AP* samples. Qualitatively, we observe that the spectra for the MnZn06 *AP* and *HT* samples are quite similar. By comparison, we also see that the spectra of these samples are different from those obtained for $ZnMn_2O_4$ and MnO; otherwise, they correspond

reasonably well to the spectrum acquired for the undoped ZnO reference sample at the Zn *K*-edge. This result again lets us infer that the main fraction of the Mn^{2+} ions in the MnZn06 *AP* and *HT* samples is located at the sites of Zn^{2+} ions in the *w*-ZnO lattice. The situation is different for the other samples. As observed via XANES for the *AP* samples, as *x* increases, the obtained spectrum for each sample increasingly resembles the spectrum for the reference powder $ZnMn_2O_4$. Similarly, for the *HT* samples, as *x* increases, the spectra became similar to that for the reference powder MnO.

Theoretical simulations of the measured Fourier transforms for the MnZn06 *AP* and *HT* samples were also performed (symbols in Fig. 6). The technical details of the theoretical analysis were described in Ref. 18. Single and multi-scattering paths corresponding to the four successive atomic shells around Mn placed at the Zn sites of the ZnO structure were considered according to the hexagonal wurtzite with $P6_3mc$ space group. The parameters obtained via simulations are shown in Table 3. The obtained quality factor indicates the good reliability of the fits, which is confirmed by the comparison of the experimental (lines) and the fitted (symbols) data in Fig. 6. These results also confirm that the Mn^{2+} ions in the MnZn06 *AP* and *HT* samples take the place of the Zn^{+2} ions in the *w*-ZnO lattice. Important and additional information can be extracted from the coordination number (*N*). For the first coordination shells, *N* decreases from the *AP* to *HT* sample, which indicates an increase in vacancies as a function of the heat treatment, confirming also the previous assumptions regarding the efficiency of the heat treatment to induce these defects into the *w*-ZnO lattice.

3.5. Magnetometry

The SQUID measurements were performed only for the MnZn06 (free of secondary phases) and MnZn11 (with a low amount of secondary phases) *AP* and *HT* samples. All *M*(*H*) curves (not shown) present paramagnetic (PM) behavior with a positive slope. No trace of ferromagnetic order is detected even at low temperatures. However, as we have undoubtedly shown in the previous sections, V_O are induced in our samples via the heat treatment in the reducing atmosphere, and, in spite of this, only PM behavior is observed.

Several authors have reported RTFM in single-phase $Zn_{1-x}Mn_xO$ samples after heat treatment in reducing atmospheres [33–35,76] and all of them claim that V_O are the defects that couple to the Mn^{2+} ions into the *w*-ZnO lattice. In contrast, our findings are supported by other reports [18,55,56,77], which show that heat treatment in a reducing atmosphere cannot lead to the desired ferromagnetic behavior. In this scenario and considering our results, we conclude that, at least for the Mn-doped *w*-ZnO system, V_O are not the necessary defects for achieving the RTFM. Following the results of Kittilstved et al. [78], Mn-doped *w*-ZnO presents RTFM only under *p*-type conduction; therefore, since V_{Zn} is a shallow acceptor defect and can also form polarons, we can state that V_{Zn} is a better candidate to promote ferromagnetic coupling between the Mn^{2+} ions.

Table 3
Mn *K*-edge EXAFS simulation results obtained by assuming Mn^{2+} at Zn^{2+} sites in the *w*-ZnO lattice for the MnZn06 ($x = 0.06$) *AP* and *HT* samples. *R* is the distance from the central atom, *N* is the average coordination number, σ^2 the Debye-Waller factor and *QF* the quality factor.

Sample	Shell	*R* (Å)	*N*	σ^2 (Å^2)	*QF*
MnZn06 (*AP*)	Mn-O	2.04(1)	4.3(6)	0.007(2)	3.02
	Mn-Zn	3.28(1)	6.1(7)	0.010(1)	
	Mn-Zn	3.22(2)	4.0(6)	0.010(1)	
	Mn-O	3.81(3)	6(1)	0.007(2)	
MnZn06 (*HT*)	Mn-O	2.03(1)	3.8(6)	0.005(2)	4.01
	Mn-Zn	3.27(2)	5(2)	0.009(2)	
	Mn-Zn	3.22(1)	4(1)	0.009(2)	
	Mn-O	3.85(4)	6(2)	0.005(2)	

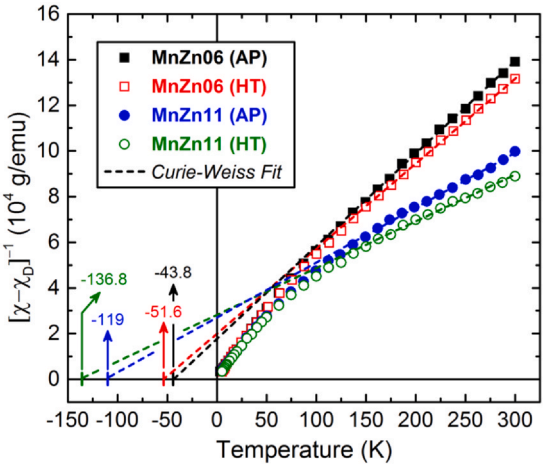

Fig. 7. Inverse susceptibility as a function of temperature for the MnZn06 and MnZn11 *AP* and *HT* samples. The best fit of the high-temperature data to the Curie-Weiss law is shown as dashed lines. The diamagnetic background of the *w*-ZnO matrix (χ_D) was subtracted from the raw data.

The inverse of the *dc* magnetic susceptibilities (χ^{-1}) as a function of temperature are presented in Fig. 7. In the high-temperature range (100–300 K), χ^{-1} presents a typical linear Curie-Weiss behavior. Below 100 K, χ^{-1} deviates from the linear dependence toward zero due to the effect of the ground states of Mn clusters coupled by antiferromagnetic interactions [79]. This feature was also reported for different TM-doped *w*-ZnO materials [80] and also for different DMSs [81–83]. In the Curie-Weiss law, the *dc* magnetic susceptibility (χ) as a function of temperature (*T*) is given as $\chi(T) = C/(T - \theta)$, where *C* is the Curie constant per gram and θ is the Curie-Weiss temperature.

The obtained parameters from the fitting of the experimental data in Fig. 7 are presented in Table 4. A negative θ was obtained, which is confirmation of a large antiferromagnetic (AF) interaction between Mn ions in the tested samples. We draw attention to the fact that only slight differences can be observed between the *AP* and *HT* samples (Fig. 7 and fit parameters in Table 4). This result indicates that the heat treatment does not considerably affect the magnetic properties of the samples, even considering the secondary phase transition from $ZnMn_2O_4$ (*AP*) to $Mn_{1-x}Zn_xO$ (*HT*) for the MnZn11 sample. In fact, both secondary phases present AF behavior between the Mn ions in their structures.

Bulk MnO was one of the first studied AF materials using neutron scattering and its magnetic properties can be easily found with $\theta = -600$ K and a Néel temperature of $T_N = 118$ K [84]. Furthermore, the magnetic properties of ZnM_2O_4 are not completely understood; nevertheless, there is a consensus that it is also an AF material with $\theta = -333$ K and a Néel temperature (still under debate) ranging from 15 K [73] to 297 K [85]. Here, we could not observe in the susceptibility measurements for the MnZn11 samples any evidence of a PM-AF transition, most probably due to the low amount of the secondary phases present in these samples (~3%, Table S1). However, based on

Table 4
Parameters determined from magnetic measurements. *C* is the Curie constant per gram, θ is the Curie-Weiss temperature, x_M is the Mn concentration of the paramagnetic phase and J_1/k_B is the effective exchange integral constant between the nearest neighbors.

Sample	*C* (10^{-3} emu K g^{-1})	θ (K)	x_M (%) ($S = 5/2$)	J_1/k_B (K)
MnZn06 (AP)	2.5(1)	− 43.8(6)	0.0456(5)	− 13.7(6)
MnZn06 (HT)	2. 2(1)	− 51.6(6)	0.0492(5)	− 15.0(6)
MnZn11 (AP)	4.3(2)	− 119(1)	–	–
MnZn11 (HT)	4.9(2)	− 136.8(8)	–	–

the available magnetic data for these materials, we can interpret the relative increase of the strength of θ for the *HT* samples to the presence of MnO in these samples, which has a higher AF coupling between the Mn ions than that for $ZnMn_2O_4$.

The Mn ion concentration (x_M) for the single-phase samples ($x = 0.06$) was determined from the *C* value obtained through the Curie-Weiss fit and the relation $C = x_M N(g\mu_B)^2 S(S+1)/3k_B$, where *N* is the number of cations per gram, *g* and *S* are the Landé factor and the spin of the Mn ions ($g = 2.0016$ and $S = 5/2$), respectively [86], μ_B is the Bohr magneton and k_B is the Boltzman constant. An estimation of the nearest neighbor exchange constant J_1 can be made using $\theta_0 = x_M 2zS(S+1)J_1/3k_B$, where *z* is the coordination number of the nearest neighbors ($z = 12$). The obtained values for x_M are in good agreement with the measured Mn concentration presented before (x_E and x_R). The J_1/k_B values are also consistent with previous results on $Zn_{1-x}Mn_xO$ bulk samples [50,87,88].

4. Conclusions

In summary, we have presented a systematic microstructural and magnetic characterization of MnO:ZnO polycrystalline bulk samples prepared via a standard solid-state reaction method. The structural results confirm the incorporation of Mn^{2+} ions up to ~8.5 at% (average value in Table 1) and indicate that it takes place mainly at the surface of the *w*-ZnO grains. For samples with higher *x*, the secondary phases $ZnMn_2O_4$ and $Mn_{1-x}Zn_xO$ were detected for the *AP* and *HT* samples, respectively. It was directly confirmed that the heat treatment is efficient in reducing the Mn ions, Mn^{3+} to Mn^{2+}, and in introducing V_O into the system. For the sample of the lower *x*, in spite of the Mn^{2+} doping of the *w*-ZnO lattice and the induced V_O via heat treatment, the magnetometry results only show PM behavior with an AF coupling among the Mn^{2+} ions, without any trace of the often-reported RTFM. When considering the BMP model, we can state that V_O cannot be addressed to the defect responsible for the magnetic coupling between Mn^{2+} into the Mn-doped *w*-ZnO lattice.

CRediT authorship contribution statement

V.M. Almeida Lage: Investigation, Writing - review. **R.T. da Silva**: Investigation, Writing - review. **A. Mesquita**: Investigation, Writing - review. **M.P.F. de Godoy**: Investigation, Writing - review. **X. Gratens**: Investigation, Writing - review. **V.A. Chitta**: Investigation, Writing - review. **H.B. de Carvalho**: Conceptualization, Supervision, Project administration, Investigation, Writing - original draft.

Declaration of Competing Interest

The authors declare that they have no known competing financial interests or personal relationships that could have appeared to influence the work reported in this paper.

Acknowledgments

Support from CNPq (grant 306715/2018-0) and FAPESP (07/56231-0; grant 2015/16191-5) is gratefully acknowledged. This research used the resources of the Brazilian Synchrotron Light Laboratory (LNLS), an open national facility operated by the Brazilian Centre for Research in Energy and Materials (CNPEM) for the Brazilian Ministry for Science, Technology, Innovations and Communications (MCTIC). The XAFS2 beamline staff are acknowledged for assistance during the experiments.

Appendix A. Supporting information

Supplementary data associated with this article can be found in the online version at doi:10.1016/j.jallcom.2020.158320.

References

[1] E. Fortunato, A. Goncalves, A. Pimentel, P. Barquinha, G. Goncalves, L. Pereira, I. Ferreira, R. Martins, Zinc oxide, a multifunctional material: from material to device applications, Appl. Phys. A Mater. Sci. Process. 96 (1) (2009) 197–205.
[2] J. Grottrup, I. Paulowicz, A. Schuchardt, V. Kaidas, S. Kaps, O. Lupan, R. Adelung, Y.K. Mishra, Three-dimensional flexible ceramics based on interconnected network of highly porous pure and metal alloyed ZnO tetrapods, Ceram. Int. 42 (7) (2016) 8664–8676.
[3] A. Teke, U. Ozgur, S. Dogan, X. Gu, H. Morkoc, B. Nemeth, J. Nause, H.O. Everitt, Excitonic fine structure and recombination dynamics in single-crystalline ZnO, Phys. Rev. B 70 (19) (2004) 195207.
[4] R. Ullah, J. Dutta, Photocatalytic degradation of organic dyes with manganese-doped ZnO nanoparticles, J. Hazard. Mater. 156 (1–3) (2008) 194–200.
[5] M. Ohtaki, Recent aspects of oxide thermoelectric materials for power generation from mid-to-high temperature heat source, J. Ceram. Soc. Jpn. 119 (1395) (2011) 770–775.
[6] D.T. Phan, G.S. Chung, Surface acoustic wave hydrogen sensors based on ZnO nanoparticles incorporated with a Pt catalyst, Sens. Actuators B Chem. 161 (1) (2012) 341–348.
[7] P. Nunes, E. Fortunato, A. Lopes, R. Martins, Influence of the deposition conditions on the gas sensitivity of zinc oxide thin films deposited by spray pyrolysis, Int. J. Inorg. Mater. 3 (8) (2001) 1129–1131.
[8] B. Kumar, S.W. Kim, Energy harvesting based on semiconducting piezoelectric ZnO nanostructures, Nano Energy 1 (3) (2012) 342–355.
[9] H.L. Tuller, S.R. Bishop, Point defects in oxides: tailoring materials through defect engineering, Annu. Rev. Mater. Res. 41 (2011) 369–398.
[10] H.M. Xiong, ZnO nanoparticles applied to bioimaging and drug delivery, Adv. Mater. 25 (37) (2013) 5329–5335.
[11] S.B. Rana, R.P.P. Singh, Investigation of structural, optical, magnetic properties and antibacterial activity of Ni-doped zinc oxide nanoparticles, J. Mater. Sci. Mater. Electron. 27 (9) (2016) 9346–9355.
[12] I. Zutic, J. Fabian, S. Das, Sarma, spintronics: fundamentals and applications, Rev. Mod. Phys. 76 (2) (2004) 323–410.
[13] T. Dietl, H. Ohno, F. Matsukura, J. Cibert, D. Ferrand, Zener model description of ferromagnetism in zinc-blende magnetic semiconductors, Science 287 (5455) (2000) 1019–1022.
[14] N. Khare, M.J. Kappers, M. Wei, M.G. Blamire, J.L. MacManus-Driscoll, Defect-induced ferromagnetism in Co-doped ZnO, Adv. Mater. 18 (11) (2006) 1449–1452.
[15] E.Z. Liu, Y. He, J.Z. Jiang, Ferromagnetism induced by defect complex in Co-doped ZnO, Appl. Phys. Lett. 93 (13) (2008) 132506.
[16] M.P.F. de Godoy, A. Mesquita, W. Avansi, P.P. Neves, V.A. Chitta, W.B. Ferraz, M.A. Boselli, A.C.S. Sabioni, H.B. de Carvalho, Evidence of defect-mediated magnetic coupling on hydrogenated Co-doped ZnO, J. Alloy. Compd. 555 (2013) 315–319.
[17] N.C. Mamani, R.T. da Silva, A.O. de Zevallos, A.A.C. Cotta, W.A.D. Macedo, M.S. Li, M.I.B. Bernardi, A.C. Doriguetto, H.B. de Carvalho, On the nature of the room temperature ferromagnetism in nanoparticulate co-doped ZnO thin films prepared by EB-PVD, J. Alloy. Compd. 695 (2017) 2682–2688.
[18] V.M. de Almeida, A. Mesquita, A.O. de Zevallos, N.C. Mamani, P.P. Neves, X. Gratens, V.A. Chitta, W.B. Ferraz, A.C. Doriguetto, A.C.S. Sabioni, H.B. de Carvalho, Room temperature ferromagnetism promoted by defects at zinc sites in Mn-doped ZnO, J. Alloy. Compd. 655 (2016) 406–414.
[19] W.S. Yan, Z.H. Sun, Q.H. Liu, Z.R. Li, Z.Y. Pan, J. Wang, S.Q. Wei, D. Wang, Y.X. Zhou, X.Y. Zhang, Zn vacancy induced room-temperature ferromagnetism in Mn-doped ZnO, Appl. Phys. Lett. 91 (6) (2007) 062113.
[20] S. Chattopadhyay, S.K. Neogi, A. Sarkar, M.D. Mukadam, S.M. Yusuf, A. Banerjee, S. Bandyopadhyay, Defects induced ferromagnetism in Mn doped ZnO, J. Magn. Magn. Mater. 323 (3–4) (2011) 363–368.
[21] T.S. Herng, S.P. Lau, S.F. Yu, J.S. Chen, K.S. Teng, Zn-interstitial-enhanced ferromagnetism in cu-doped ZnO films, J. Magn. Magn. Mater. 315 (2) (2007) 107–110.
[22] M. Ivill, S.J. Pearton, S. Rawal, L. Leu, P. Sadik, R. Das, A.F. Hebard, M. Chisholm, J.D. Budai, D.P. Norton, Structure and magnetism of cobalt-doped ZnO thin films, New J. Phys. 10 (2008) 065002.
[23] S. Ramachandran, J. Narayan, J.T. Prater, Effect of oxygen annealing on Mn doped ZnO diluted magnetic semiconductors, Appl. Phys. Lett. 88 (24) (2006) 242503.
[24] D.C. Kundaliya, S.B. Ogale, S.E. Lofland, S. Dhar, C.J. Metting, S.R. Shinde, Z. Ma, B. Varughese, K.V. Ramanujachary, L. Salamanca-Riba, T. Venkatesan, On the origin of high-temperature ferromagnetism in the low-temperature-processed Mn-Zn-O system, Nat. Mater. 3 (10) (2004) 709–714.
[25] W.B. Mi, H.L. Bai, H. Liu, C.Q. Sun, Microstructure, magnetic, and optical properties of sputtered Mn-doped ZnO films with high-temperature ferromagnetism, J. Appl. Phys. 101 (2) (2007) 023904.
[26] M. El-Hilo, A.A. Dakhel, Structural and magnetic properties of Mn-doped ZnO powders, J. Magn. Magn. Mater. 323 (16) (2011) 2202–2205.
[27] Q.Q. Gao, Y.Q. Dai, C.B. Li, L.G. Yang, X.C. Li, C.J. Cui, Correlation between oxygen vacancies and dopant concentration in Mn-doped ZnO nanoparticles synthesized by co-precipitation technique, J. Alloy. Compd. 684 (2016) 669–676.

[28] X.L. Wang, C.Y. Luan, Q. Shao, A. Pruna, C.W. Leung, R. Lortz, J.A. Zapien, A. Ruotolo, Effect of the magnetic order on the room-temperature band-gap of Mn-doped ZnO thin films, Appl. Phys. Lett. 102 (10) (2013) 102112.

[29] A.K.M. Alsmadi, B. Salameh, M. Shatnawi, Influence of oxygen defects and their evolution on the ferromagnetic ordering and band gap of Mn-doped ZnO films, J. Phys. Chem. C 124 (29) (2020) 16116–16126.

[30] W. Chen, L.F. Zhao, Y.Q. Wang, J.H. Miao, S. Liu, Z.C. Xia, S.L. Yuan, Magnetism in Mn-doped ZnO bulk samples, Solid State Commun. 134 (12) (2005) 827–830.

[31] H.S. Hsu, J.C.A. Huang, Y.H. Huang, Y.F. Liao, M.Z. Lin, C.H. Lee, J.F. Lee, S.F. Chen, L.Y. Lai, C.P. Liu, Evidence of oxygen vacancy enhanced room-temperature ferromagnetism in Co-doped ZnO, Appl. Phys. Lett. 88 (24) (2006) 242507.

[32] M. Naeem, S.K. Hasanain, M. Kobayashi, Y. Ishida, A. Fujimori, S. Buzby, S.I. Shah, Effect of reducing atmosphere on the magnetism of $Zn_{1-x}Co_xO$ ($0 \le x \le 0.10$) nanoparticles, Nanotechnology 17 (10) (2006) 2675–2680.

[33] G. Glaspell, P. Dutta, A. Manivannan, A room-temperature and microwave synthesis of m-doped ZnO (M = Co, Cr, Fe, Mn & Ni), J. Clust. Sci. 16 (4) (2005) 523–536.

[34] V.K. Sharma, G.D. Varma, Oxygen vacancies induced room temperature ferromagnetism in hydrogenated Mn-doped ZnO, J. Appl. Phys. 102 (5) (2007) 056105.

[35] Z.H. Wang, D.Y. Geng, W.J. Hu, Z.D. Zhang, Raman spectra and room-temperature ferromagnetism of hydrogenated $Zn_{0.95}Mn_{0.05}O$ nanopowders, J. Appl. Phys. 105 (12) (2009) 123902.

[36] H. Zhang, S. Qin, Y.Q. Cao, Z.X. Yang, L.F. Si, W. Zhong, D. Wu, M.X. Xu, Q.Y. Xu, Enhanced room temperature ferromagnetism in hydrogenated $Zn_{0.98}Mn_{0.02}O$, Appl. Surf. Sci. 271 (2013) 421–423.

[37] D. Gaspar, L. Pereira, K. Gehrke, B. Galler, E. Fortunato, R. Martins, High mobility hydrogenated zinc oxide thin films, Sol. Energy Mater. Sol. Cells 163 (2017) 255–262.

[38] M. Lalanne, J.M. Soon, A. Barnabe, L. Presmanes, I. Pasquet, P. Tailhades, Preparation and characterization of the defect-conductivity relationship of Ga-doped ZnO thin films deposited by nonreactive radio-frequency-magnetron sputtering, J. Mater. Res. 25 (12) (2010) 2407–2414.

[39] H.W. Park, K.B. Chung, J.S. Park, A role of oxygen vacancy on annealed ZnO film in the hydrogen atmosphere, Curr. Appl. Phys. 12 (2012) S164–S167.

[40] L.S. Liu, Z.X. Mei, A.H. Tang, A. Azarov, A. Kuznetsov, Q.K. Xue, X.L. Du, Oxygen vacancies: the origin of n-type conductivity in ZnO, Phys. Rev. B 93 (23) (2016) 235305.

[41] R.H. Lamoreaux, D.L. Hildenbrand, L. Brewer, High-temperature vaporization behavior of oxides.2. Oxides of Be, Mg, Ca, Sr, Ba, B, Al, Ga, In, Tl, Si, Ge, Sn, Pb, Zn, Cd, and Hg, J. Phys. Chem. Ref. Data 16 (3) (1987) 419–443.

[42] L. Meng, M. Konagai, S. Miyajima, Effect of annealing atmosphere on the electrical and optical properties of sol-gel derived Al doped $Zn_{1-x}Mg_xO$ thin film, Thin Solid Films 597 (2015) 144–150.

[43] J.M.D. Coey, M. Venkatesan, C.B. Fitzgerald, Donor impurity band exchange in dilute ferromagnetic oxides, Nat. Mater. 4 (2) (2005) 173–179.

[44] A. Janotti, C.G. Van, Native point defects in ZnO, Phys. Rev. B 76 (16) (2007) 165202.

[45] O.F. Schirmer, O- bound small polarons in oxide materials, J. Phys. Condens. Matter 18 (43) (2006) R667–R704.

[46] S. Lany, A. Zunger, Polaronic hole localization and multiple hole binding of acceptors in oxide wide-gap semiconductors, Phys. Rev. B 80 (8) (2009) 085202.

[47] A.C. Durst, R.N. Bhatt, P.A. Wolff, Bound magnetic polaron interactions in insulating doped diluted magnetic semiconductors, Phys. Rev. B 65 (23) (2002) 235205.

[48] N. Ali, A.R. Vijaya, Z.A. Khan, K. Tarafder, A. Kumar, M.K. Wadhwa, B. Singh, S. Ghosh, Ferromagnetism from non-magnetic ions: Ag-doped ZnO, Sci. Rep. 9 (2019) 20039.

[49] R. Shannon, Revised effective ionic radii and systematic studies of interatomic distances in halides and chalcogenides, Acta Crystallogr. Sect. A 32 (5) (1976) 751–767.

[50] S. Kolesnik, B. Dabrowski, J. Mais, Structural and magnetic properties of transition metal substituted ZnO, J. Appl. Phys. 95 (5) (2004) 2582–2586.

[51] S. Kolesnik, B. Dabrowski, Absence of room temperature ferromagnetism in bulk Mn-doped ZnO, J. Appl. Phys. 96 (9) (2004) 5379–5381.

[52] A.C. Larson, R. Von Dreele, General Structure Analysis System (GSAS)(Report LAUR 86-748), Los Alamos National Laboratory, Los Alamos, New Mexico, 2004.

[53] B. Toby, EXPGUI, a graphical user interface for GSAS, J. Appl. Crystallogr. 34 (2) (2001) 210–213.

[54] S.C. Abrahams, J.L. Bernstein, Remeasurement of the structure of hexagonal ZnO, Acta Crystallogr. Sect. B 25 (7) (1969) 1233–1236.

[55] S. Kolesnik, B. Dabrowski, J. Mais, Origin of spin-glass behavior of $Zn_{1-x}Mn_xO$, J. Supercond. 15 (4) (2002) 251–255.

[56] A. Singhal, Study of hydrogenation versus de-loading of Co and Mn doped ZnO semiconductor, J. Alloy. Compd. 507 (1) (2010) 312–316.

[57] M. Rahaman, Sintering of Ceramics, CRC Press, Boca Raton, 2007.

[58] B. Straumal, B. Baretzky, A. Mazilkin, S. Protasova, A. Myatiev, P. Straumal, Increase of Mn solubility with decreasing grain size in ZnO, J. Eur. Ceram. Soc. 29 (10) (2009) 1963–1970.

[59] H.B. de Carvalho, M.P.F. de Godoy, R.W.D. Paes, M. Mir, A. Ortiz de Zevallos, F. Iikawa, M.J.S.P. Brasil, V.A. Chitta, W.B. Ferraz, M.A. Boselli, A.C.S. Sabioni, Absence of ferromagnetic order in high quality bulk Co-doped ZnO samples, J. Appl. Phys. 108 (3) (2010) 033914.

[60] T.C. Damen, S.P.S. Porto, B. Tell, Raman effect in zinc oxide, Phys. Rev. 142 (2) (1966) 570–574.

[61] R.H. Callender, S.S. Sussman, M. Selders, R.K. Chang, Dispersion of Raman cross section in CdS and ZnO over a wide energy range, Phys. Rev. B 7 (8) (1973) 3788–3798.

[62] M. Scepanovic, M. Grujic-Brojcin, K. Vojisavljevic, S. Bernik, T. Sreckovic, Raman study of structural disorder in ZnO nanopowders, J. Raman Spectrosc. 41 (9) (2010) 914–921.

[63] S. Ghose, T. Rakshit, R. Ranganathan, D. Jana, Role of Zn-interstitial defect states on d(0) ferromagnetism of mechanically milled ZnO nanoparticles, RSC Adv. 5 (121) (2015) 99766–99774.

[64] F. Friedrich, N.H. Nickel, Resonant Raman scattering in hydrogen and nitrogen doped ZnO, Appl. Phys. Lett. 91 (11) (2007) 111903.

[65] F. Reuss, C. Kirchner, T. Gruber, R. Kling, S. Maschek, W. Limmer, A. Waag, P. Ziemann, Optical investigations on the annealing behavior of gallium- and nitrogen-implanted ZnO, 2004.

[66] Z.Q. Chen, A. Kawasuso, Y. Xu, H. Naramoto, X.L. Yuan, T. Sekiguchi, R. Suzuki, T. Ohdaira, Production and recovery of defects in phosphorus-implanted ZnO, J. Appl. Phys. 97 (1) (2005) 013528.

[67] A. Mesquita, F.P. Rhodes, R.T. da Silva, P.P. Neves, A.O. de Zevallos, M.R.B. Andreeta, M.M. de Lima, A. Cantarero, I.S. da Silva, M.A. Boselli, X. Gratens, V.A. Chitta, A.C. Doriguetto, W.B. Ferraz, A.C.S. Sabioni, H.B. de Carvalho, Dynamics of the incorporation of Co into the wurtzite ZnO matrix and its magnetic properties, J. Alloy. Compd. 637 (2015) 407–417.

[68] N. Churata Mamani, R. Tomaz da Silva, A. Ortiz de Zevallos, A. Cotta, W. Augusto de Almeida Macedo, M. Li, M. Bernardi, A. Carlos Doriguetto, H. de Carvalho, On the nature of the room temperature ferromagnetism in nanoparticulate Co-doped ZnO thin films prepared by EB-PVD, 2016.

[69] R.T. da Silva, A. Mesquita, A.O. de Zevallos, T. Chiaramonte, X. Gratens, V.A. Chitta, J.M. Morbec, G. Rahman, V.M. Garcia-Suarez, A.C. Doriguetto, M.I.B. Bernardi, H.B. de Carvalho, Multifunctional nanostructured Co-doped ZnO: Co spatial distribution and correlated magnetic properties, Phys. Chem. Chem. Phys. 20 (30) (2018) 20257–20269.

[70] M. Schumm, M. Koerdel, S. Müller, H. Zutz, C. Ronning, J. Stehr, D.M. Hofmann, J. Geurts, Structural impact of Mn implantation on ZnO, New J. Phys. 10 (4) (2008) 043004.

[71] L. Malavasi, P. Galinetto, M.C. Mozzati, C.B. Azzoni, G. Flor, Raman spectroscopy of $AMn_{(2)}O_{(4)}$ (A = Mn, Mg and Zn) spinels, Phys. Chem. Chem. Phys. 4 (15) (2002) 3876–3880.

[72] J.F. Fernandez, A.C. Caballero, M. Villegas, S.J. Khatib, M.A. Banares, J.L.G. Fierro, J.L. Costa-Kramer, E. Lopez-Ponce, M.S. Martin-Gonzalez, F. Briones, A. Quesada, M. Garcia, A. Hernando, Structure and magnetism in the Zn-Mn-O system: a candidate for room temperature ferromagnetic semiconductor, J. Eur. Ceram. Soc. 26 (14) (2006) 3017–3025.

[73] H. Li, B. Song, W.J. Wang, X.L. Chen, Facile synthesis, thermal, magnetic, Raman characterizations of spinel structure ZnMn2O4, Mater. Chem. Phys. 130 (1–2) (2011) 39–44.

[74] J.M. Calleja, M. Cardona, Resonant Raman scattering in ZnO, Phys. Rev. B 16 (8) (1977) 3753–3761.

[75] L.R. Valerio, N.C. Mamani, A.O. de Zevallos, A. Mesquita, M.I.B. Bernardi, A.C. Doriguetto, H.B. de Carvalho, Preparation and structural-optical characterization of dip-coated nanostructured Co-doped ZnO dilute magnetic oxide thin films, RSC Adv. 7 (33) (2017) 20611–20619.

[76] Q.Q. Gao, Y.Q. Dai, Q.X. Yu, C.B. Li, X.C. Li, C.J. Cui, J. Zhang, H.B. Chen, Defect-induced structural and ferromagnetic properties of hydrogenated Mn-doped ZnO film, J. Mater. Sci. Mater. Electron. 27 (1) (2016) 697–704.

[77] A. Manivannan, P. Dutta, G. Glaspell, M.S. Seehra, Nature of magnetism in Co- and Mn-doped ZnO prepared by sol-gel technique, J. Appl. Phys. 99 (8) (2006) 08M110.

[78] K.R. Kittilstved, W.K. Liu, D.R. Gamelin, Electronic structure origins of polarity-dependent high-T-C ferromagnetismin oxide-diluted magnetic semiconductors, Nat. Mater. 5 (4) (2006) 291–297.

[79] J. Spalek, A. Lewicki, Z. Tarnawski, J.K. Furdyna, R.R. Galazka, Z. Obuszko, Magnetic-susceptibility of semimagnetic semiconductors - the high-temperature regime and the role of superexchange, Phys. Rev. B 33 (5) (1986) 3407–3418.

[80] S. Kolesnik, B. Dabrowski, J. Mais, Structural and magnetic properties of transition metal substituted ZnO, J. Appl. Phys. 95 (5) (2004) 2582–2586.

[81] H. Alawadhi, I. Miotkowski, A. Lewicki, A.K. Ramdas, S. Miotkowska, M. McElfresh, Magnetic susceptibility and compositional dependence of the energy gap in Cd1-xCoxTe, J. Phys. Condens. Matter 14 (17) (2002) 4611–4620.

[82] T.E. de Souza, A. Mesquita, A.O. de Zevallos, F. Beron, K.R. Pirota, P.P. Neves, A.C. Doriguetto, H.B. de Carvalho, Structural and magnetic properties of dilute magnetic oxide based on nanostructured Co-doped anatase TiO2 ($Ti_{1-x}Co_xO_{2-\delta}$), J. Phys. Chem. C 117 (25) (2013) 13252–13260.

[83] M.I.B. Bernardi, A. Mesquita, F. Beron, K.R. Pirota, A.O. de Zevallos, A.C. Doriguetto, H.B. de Carvalho, The role of oxygen vacancies and their location in the magnetic properties of $Ce_{1-x}Cu_xO_{2-\delta}$ nanorods, Phys. Chem. Chem. Phys. 17 (5) (2015) 3072–3080.

[84] B.D. Cullity, C.D. Graham, Introduction of Magnetic Materials, John Wiley & Sons Inc,, Hoboken, New Jersey, 2009.

[85] P. Patra, I. Naik, H. Bhatt, S.D. Kaushik, Structural, infrared spectroscopy and magnetic properties of spinel ZnMn2O4, Phys. B Condens. Matter 572 (2019) 199–202.

[86] P.B. Dorain, Electron paramagnetic resonance of manganese(II) in hexagonal zinc oxide and cadmium sulfide single crystals, Phys. Rev. 112 (4) (1958) 1058–1060.

[87] T. Fukumura, Z.W. Jin, M. Kawasaki, T. Shono, T. Hasegawa, S. Koshihara, H. Koinuma, Magnetic properties of mn-doped ZnO, Appl. Phys. Lett. 78 (7) (2001) 958–960.

[88] X. Gratens, V. Bindilatti, N.F. Oliveira, Y. Shapira, S. Foner, Z. Golacki, T.E. Haas, Magnetization steps inZn1−xMnxO: four largest exchange constants and single-ion anisotropy, Phys. Rev. B 69 (12) (2004) 125209.